

Quantifying and Reducing Model-Form Uncertainties in Reynolds-Averaged Navier–Stokes Equations: An Open-Box, Physics-Based, Bayesian Approach

H. Xiao*, J.-L. Wu, J.-X. Wang, R. Sun, C. J. Roy

Department of Aerospace and Ocean Engineering, Virginia Tech, Blacksburg, VA 24060, United States

Abstract

Despite their well-known limitations, Reynolds-Averaged Navier–Stokes (RANS) models are still the workhorse tools for turbulent flow simulations in today’s engineering analysis, design and optimizations. While the predictive skills of RANS models depend on many factors, for many practical flows the turbulence models are by far the most important source of uncertainty. As RANS models are used in the design and safety evaluation of many mission-critical systems such as airplanes and nuclear power plants, quantifying their model-form uncertainties has significant implications in enabling risk-informed decision-making. In this work we develop an open-box, physics-informed Bayesian framework for quantifying model-form uncertainties in RANS simulations. Uncertainties are introduced directly to the Reynolds stresses and are represented with compact parameterization accounting for empirical prior knowledge and physical constraints (e.g., realizability, smoothness, and symmetry). An iterative ensemble Kalman method is used to assimilate the prior knowledge and observation data in a Bayesian framework, and to propagate them to posterior distributions of velocities and other Quantities of Interest (QoIs). We use two representative cases, the flow over periodic hills and the flow in a square duct, to evaluate the performance of the proposed framework. Both cases are challenging for the commonly used turbulence models. Simulation results suggest that, even with very sparse observations, the obtained posterior mean velocities and other QoIs have significantly better agreement with the benchmark data compared to the baseline results. At most locations the posterior distribution adequately represents the model-form uncertainties. The framework is a major improvement over existing black-box, physics-neutral methods for model-form uncertainty quantification, where

*Corresponding author. Tel: +1 540 231 0926

Email address: hengxiao@vt.edu (H. Xiao)

prior knowledge and details of the models are not exploited. This approach has potential implications in many fields beyond turbulence modeling. A notable example is climate modeling, where high-consequence decisions are made based on predictions (e.g., projected temperature rise) with major uncertainties originating from closure models that are used to account for unresolved or unknown physics including radiation, cloud, and boundary layer processes.

Keywords: uncertainty quantification, ensemble Kalman filtering, turbulence modeling, Reynolds-Averaged Navier–Stokes equations

1. Introduction

1.1. Model-Form Uncertainties in RANS-Based Turbulence Modeling

In Computational Fluid Dynamics (CFD), the Reynolds-Averaged Navier-Stokes (RANS) solvers are still the workhorse tool for turbulent flow simulations in today’s engineering analysis, design and optimizations, despite their well-known limitations, e.g., poor performance in flows with separation, mean pressure gradient, and mean flow curvature [1]. This is due to the fact that high-fidelity models such as Large Eddy Simulation (LES) and Direct Numerical Simulation (DNS) are still prohibitively expensive for engineering systems of practical interests. Moreover, in engineering designs and optimizations, many simulations must be performed with short turn-around times, which preclude the use of these high fidelity models.

The RANS equations employ a time- or ensemble-averaging process to eliminate temporal dependency for stationary turbulence. The averaging leads to an unclosed correlation term, the Reynolds stress, which needs to be modeled with turbulence models [1, 2]. Turbulence modeling is a primary source of uncertainty in the CFD simulations of turbulent flows. Tens of turbulence models have been proposed so far. Each has better performance in certain cases yet none is convincingly superior to others in general. This is due to the fact that the empirical closure models cannot accurately model the regime-dependent, physics-rich phenomena of turbulent flows. Predictions obtained with any of these models have uncertainties that are difficult to quantify. The model-form uncertainties in RANS simulations originating from the turbulence models are the main focus of this work.

1.2. Model-Form Uncertainty Quantification: Existing Approaches

A traditional approach for estimating RANS modeling uncertainties involves repeating the simulations by perturbing the coefficients used in the turbulence models, or by using

several different turbulence models [3] (e.g., k - ε , k - ω , and Spalart–Allmaras models [1]) and observe the sensitivity of the Quantities of Interests (QoIs). However, different models are often based on similar approximations, and they are likely to share similar biases [4]. Consequently, this *ad hoc* model ensemble approach tends to underestimate of the uncertainty in the model. In turbulence modeling, the Boussinesq assumption states that the Reynolds stress tensor is aligned with and proportional to the local traceless mean strain rate tensor. This assumption is shared by all eddy-viscosity models, including the three classes of commonly used models mentioned above.

In their seminal work, Kennedy and O’Hagan [5] developed a Bayesian calibration approach which includes a model discrepancy term to account for Model-Form Uncertainty (MFU). In this approach the MFU is quantified by parameterizing the difference between the *outputs* of the computational model and experimental observations as a stationary Gaussian process whose hyperparameters can be inferred from data [5]. This framework has been used in many applications, and a number of sophisticated variants have been developed, e.g., by introducing non-stationary Gaussian processes to model the discrepancy [6], using multiplicative discrepancy term [7], or using high-fidelity models and field measurements to provide observation data [7–10]. While this approach has had some success, the physics-neutral approach treats the entire numerical model as a black box and does not exploit the prior information which often exists about the nature of the MFU in a given model. Moreover, this framework addresses MFU only in terms of the QoIs, whereas the modeling errors in RANS simulation arise specifically from the modeled Reynolds stress term. Recent work of Brynjarsdottir and O’Hagan [11] emphasized the importance of incorporating prior information, but also highlighted the difficulties of enforcing prior information in this black-box framework. Even a simple constraint such as zero-gradient boundary condition on the discrepancy is challenging to enforce as shown in [11]. Realistic prior knowledge in engineering practice is much more complicated.

Recently, several prominent groups in the CFD community (e.g., Moser and co-workers [12–14], Iaccarino and co-workers [15–19], and Dow and Wang [20]) have recognized the limitations of the black-box approach, and attempted to open the box by injecting the uncertainties locally on the closure models, and not on the model output directly. Works from these groups will be reviewed in detailed below. These approaches have some similarities to earlier work of Berliner et al. [21, 22] in the context of geophysical fluid dynamics, where uncertainties were introduced to the discretized coefficients of the governing geostrophic equations.

Moser and co-workers [12–14] are the first to explicitly point out and utilize the “com-

posite nature” of the RANS equations. That is, the equations are based on reliable theories describing conservation of mass, momentum, and energy, but contain approximate embedded models to account for the unresolved or unknown physics, i.e., the Reynolds stress terms. Based on this insight, they introduced a Reynolds stress discrepancy tensor ϵ , which is added to the modeled Reynolds stress ($\tilde{\tau}^{rans}$) in the RANS equations to account for the uncertainty due the modeling of $\tilde{\tau}^{rans}$. Stochastic differential equations forced by Wiener processes are formulated for the discrepancy ϵ . These equations are structurally similar to but simpler than the Reynolds stress transport equations commonly used in turbulence modeling [e.g., 1, 23]. Applications to plane channel flows (where on the plane shear component of the Reynolds stress tensor is important) at various Reynolds numbers have shown promising results, while extensions to general three-dimensional flows are underway (Moser and Oliver, personal communication).

Iaccarino and co-workers [15–19] proposed a framework to estimate the model-form uncertainty in RANS modeling by perturbing the Reynolds stress towards their limiting states within the physically realizable range. Empirical indicator functions are used to ensure the spatial smoothness of the perturbations in the physical domain, and to inject uncertainties only to the regions where the baseline turbulence model is believed to perform poorly. The novelty of their framework is that both physical realizability and spatial smoothness are accounted for, which are two pieces of critical prior information in turbulence modeling. Another advantage of their framework is the moderate computational overhead, since only a few limiting states of the Reynolds stresses are computed. On the other hand, it should be noted that the obtained scattering of the states can only serve as an empirical estimation of the uncertainties, and are not guaranteed to cover the truth. While the true Reynolds stress is a convex linear combination of the Reynolds stresses in the limiting states, the true velocities or other QoIs are not necessarily linear combinations of their respective limiting states.

Dow and Wang [20] quantified model-form uncertainties in the k - ω model by finding the eddy viscosity field that minimizes the misfit in the computed velocity field compared to the DNS data. While their approach has some similarities with that of Iaccarino et al., the most notable difference is that uncertainties are injected to the eddy viscosity and not to the Reynolds stresses directly. Another key difference is that they used DNS data, while Iaccarino et al. did not and instead focused only on forward propagation of uncertainties in the Reynolds stress.

In summary, the CFD community has recognized the advantages of open-box approaches

for quantifying model-form uncertainties in RANS simulations, and promising results have been obtained. However, much work is still needed.

1.3. Objective and Novelty of the Present Work

In this work, we focus on a scenario where some limited amounts of data (usually from measurements at a few locations) are available. This is often the case when CFD is used in practical applications in conjunction with real-time data to provide predictions. Examples include prediction of flows in a wind farm and atmospheric pollutant dispersion in a city [15]. Built on existing insights and experiences in the literature, the objective of this work is to develop a rigorous, open-box, physics-informed framework for quantifying model-form uncertainties in RANS simulations. The novelty of our approach is that an ensemble-based Bayesian inference method is used to incorporate all sources of available information including empirical prior knowledge, physical constraints (e.g., realizability, smoothness, and symmetric), and available observation data.

The rest of the paper is organized as follows. The model-form uncertainty quantification framework is introduced in Section 2, and numerical implementation details are given in Section 3. Numerical results for two application cases, the flow over periodic hills and the flow in a square duct, are presented in Section 4 to assess the merits and limitations of the developed framework. The success, limitations, practical significance, and possible extensions of the proposed method are further discussed in Section 5. Finally, Section 6 concludes the paper.

2. Proposed Framework

2.1. Prior Knowledge in RANS Modeling

An important feature of the proposed framework is the explicit, straightforward representation of prior knowledge in a Bayesian inference framework. As such, we summarize the prior knowledge in RANS-based turbulent flow simulations below, some of which has been reviewed in Section 1:

1. *Composite model*: The uncertainties in the modeled Reynolds stresses are the main source uncertainties in the RANS model predictions [12].
2. *Physical realizability*: The true Reynolds stress at any point in the domain resides in a subspace of a six-dimensional space [18, 24].
3. *Spatial smoothness*: The Reynolds stress field usually has smooth spatial distributions except across certain discontinuous features (e.g., shocks and abrupt changes of geometry).

4. *Problem-specific prior knowledge:* There are some well-known scenarios where eddy viscosity models are expected to perform poorly as enumerated above, e.g., flow separation, mean flow curvature. Taking the flow over periodic hills as shown in Fig. 3 for example, the flood contour indicates typical prior knowledge of the relative magnitude of the Reynolds stress discrepancies in each region, i.e., the regions with recirculation, non-parallel free-shear flow, and the strong mean flow curvature have larger discrepancies.

2.2. Representations of Prior Knowledge in the Modeling Framework

In light of the prior knowledge presented above and based on existing methods in the literature [12, 18, 20], we make the following modeling choices to represent the prior knowledge.

2.2.1. Composite model

The true Reynolds stress $\boldsymbol{\tau}$ is modeled as random field of symmetric tensors with $\tilde{\boldsymbol{\tau}}^{rans}$ as its deterministic mean field, where $\tilde{\boldsymbol{\tau}}^{rans}$ is the Reynolds stress field given in the baseline RANS simulation whose model-form uncertainty is to be quantified.¹

2.2.2. Physical realizability of Reynolds stresses

To ensure physical realizability of its realizations, the value of the Reynolds stress field $\boldsymbol{\tau}$ at any given location x is projected onto a space with six physically meaningful dimensions via the following eigen-decomposition [15, 18]:

$$\boldsymbol{\tau} = 2k \left(\frac{1}{3}\mathbf{I} + \mathbf{a} \right) = 2k \left(\frac{1}{3}\mathbf{I} + \mathbf{V}\Lambda\mathbf{V}^T \right) \quad (1)$$

where k is the turbulent kinetic energy, \mathbf{a} is the anisotropy tensor, $\mathbf{V} = [v_1, v_2, v_3]$, and $\Lambda = \text{diag}[\lambda_1, \lambda_2, \lambda_3]$ are its orthonormal eigenvectors and eigenvalues, respectively, with $\lambda_1 + \lambda_2 + \lambda_3 = 0$. This decomposition transforms the Reynolds stress to a space represented by six variables with clear physical interpretations: magnitude (represented by the turbulent kinetic energy k , which must be non-negative), shape (represented by two scalars λ_1, λ_2), and orientation (represented by three mutually orthonormal vectors² $\mathbf{v}_1, \mathbf{v}_2$, and \mathbf{v}_3) of the Reynolds stress tensor [15, 25]. Further, λ_1, λ_2 , and λ_3 are transformed to the Barycentric

¹We use \sim to emphasize the fact that $\tilde{\boldsymbol{\tau}}^{rans}$ is a deterministic field, which is in contrast to the random field $\boldsymbol{\tau}$.

²They can be considered as the three orthogonal axes of an ellipsoid, and thus the three vectors have three degrees of freedom in total, i.e., its orientation in three-dimensional space.

coordinate (C_1, C_2, C_3) , with $C_1 + C_2 + C_3 = 1$, and subsequently to the natural coordinate (ξ, η) . With the mapping from Barycentric coordinate to natural coordinate (see Fig. 1), the physically realizable turbulent stresses enclosed in the Barycentric triangle (panel a) is transformed to a square (panel b), i.e., $\{(\xi, \eta) | \xi \in [-1, 1], \eta \in [-1, 1]\}$, which is more convenient for parameterization. Details of the mapping are presented in Appendix A. In summary, we transform the Reynolds stress tensor to six physical dimensions denoted as $(k, \xi, \eta, \mathbf{v}_1, \mathbf{v}_2, \mathbf{v}_3)$. All mappings involved are linear and invertible except for a trivial singular point in $(C_1, C_2, C_3) \mapsto (\xi, \eta)$.

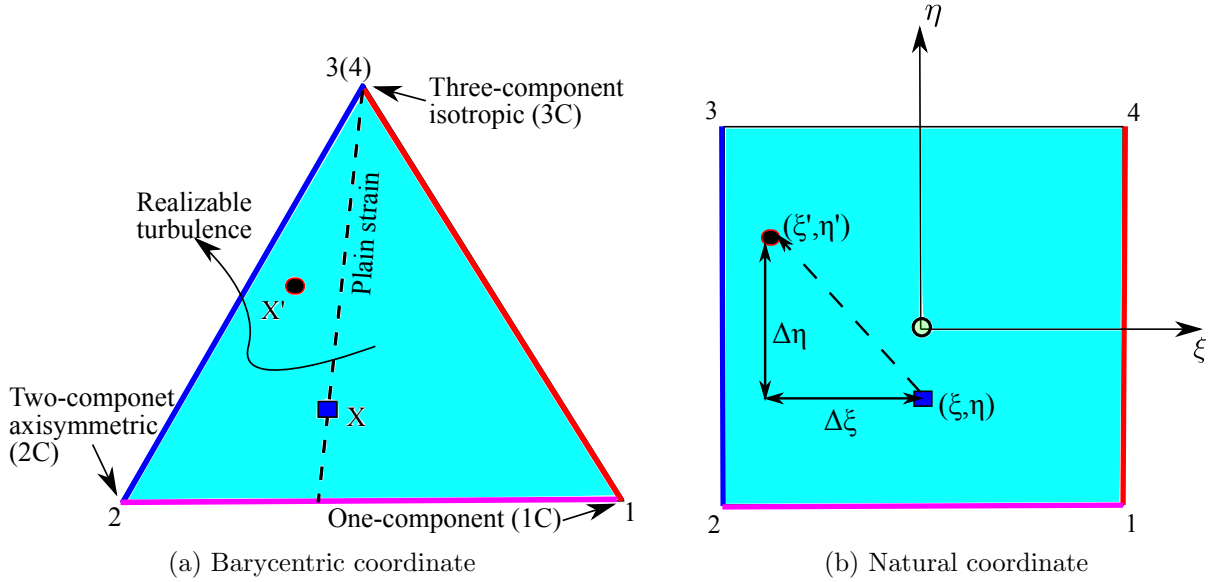


Figure 1: Mapping between the Barycentric coordinate to the natural coordinate, transforming the Barycentric triangle enclosing all physically realizable states [17, 25] to a square via standard finite element shape functions (detailed in Appendix A). Corresponding edges in the two coordinates are indicated with matching colors. The singular point 3(4) in the Barycentric coordinate, which maps to the edge 3–4 in the natural coordinate, does not pose any practical difficulties.

After the mapping of Reynolds stress $\tilde{\tau}^{rans}$ to the physically meaningful dimensions, i.e., k, ξ, η , uncertainties are injected to the projected space on these variables. This is achieved by modeling the corresponding truths δ^k, δ^ξ , and δ^η as random fields with $\tilde{k}^{rans}(x), \tilde{\xi}^{rans}(x), \tilde{\eta}^{rans}(x)$,

and $\tilde{\eta}^{rans}(x)$ as priors. Specifically,

$$k(x) = \tilde{k}^{rans}(x) \exp[\delta^k(x)] \quad (2a)$$

$$\xi(x) = \tilde{\xi}^{rans}(x) + \delta^\xi(x) \quad (2b)$$

$$\eta(x) = \tilde{\eta}^{rans}(x) + \delta^\eta(x) \quad (2c)$$

where the spatial coordinate x is the index of the random fields. Note that the multiplicative discrepancy of the turbulent kinetic energy is modeled as $\exp[\delta^k(x)]$ in Eq. (2a) to ensure the non-negativity of k , provided that the turbulent kinetic energy field $\tilde{k}^{rans}(x)$ obtained from the RANS model is non-negative.

Perturbing the orientations of the modeled Reynolds stress tensor can potentially lead to reverse diffusion in the RANS momentum equations and thus causes instability (Iaccarino, personal communication). Consistent with the work of Iaccarino et al., we focus on the magnitude (k) and the shape (λ_1 and λ_2 , or equivalently the natural coordinates ξ and η) of the Reynolds stress tensor $\boldsymbol{\tau}$, and do not introduce uncertainties into the orientations ($\mathbf{v}_1, \mathbf{v}_2, \mathbf{v}_3$).

2.2.3. Spatial smoothness of Reynolds stress distribution

To ensure spatial smoothness and to reduce the dimension of the uncertainty space, the random fields to be inferred, i.e., δ^k , δ^ξ , and δ^η , are projected to a deterministic functional basis set $\{\phi_i(x)\}$. That is,

$$\delta^k(x, \theta^k) = \sum_{i=1}^{\infty} \omega_i^k|_{\theta^k} \phi_i(x) \quad (3a)$$

$$\delta^\xi(x, \theta^\xi) = \sum_{i=1}^{\infty} \omega_i^\xi|_{\theta^\xi} \phi_i(x) \quad (3b)$$

$$\delta^\eta(x, \theta^\eta) = \sum_{i=1}^{\infty} \omega_i^\eta|_{\theta^\eta} \phi_i(x) \quad (3c)$$

where the coefficients of the i^{th} mode ω_i^k , ω_i^ξ , and ω_i^η are random variables³ depending on the realization of the random variables θ^k , θ^ξ , and θ^η , respectively, and $\phi_i(x)$ are deterministic spatial basis functions. An orthogonal basis set is chosen in this work as will be detailed below, but the orthogonality is not mandatory.

³Throughout the manuscript, subscripts denotes indices, and superscripts indicate explanation of the variable. For example, ω_i^k is the coefficient for the i^{th} mode in the expansion of the discrepancy field δ^k for the turbulent kinetic energy k . Tensors are denoted in bold (e.g., $\boldsymbol{\tau}$) and not with index notation.

Remarks: The mapping in Section 2.2.2 involves linear transformation of the Reynolds stress at a given point to physical variable spaces, which facilitate ensuring the physical realizability of the Reynolds stresses in the prior. The orthogonal projection in Section 2.2.3 aims to represent the spatial distribution function on a basis set in a compact manner, which helps ensure spatial smoothness and reduce uncertainty dimensions of $\boldsymbol{\tau}(x)$.

2.2.4. Representation of problem-specific prior knowledge

Finally, problem-specific knowledge is encoded in the choice of basis set $\{\phi_i\}$. Here we will use the flow over periodic hills as example to illustrate the representation of the problem-specific prior knowledge.

We model the prior of the discrepancies δ^k , δ^ξ and δ^η as zero-mean Gaussian random fields (also known as Gaussian processes) $\mathcal{GP}(0, K)$, where

$$K(x, x') = \sigma(x)\sigma(x') \exp\left(-\frac{|x - x'|^2}{l^2}\right) \quad (4)$$

is the kernel indicating the covariance at two locations x and x' . The variance $\sigma(x)$ is a spatially varying field specified (see the flood contour in Fig. 3) to reflect the prior knowledge that large discrepancies in modeled Reynolds stress are expected in certain regions. The correlation length scale l can be specified based on the local turbulence length scale, but is taken as constant in this work for simplicity.

The orthogonal basis functions $\phi_i(x)$ in Eq. (3) take the form $\phi_i(x) = \sqrt{\hat{\lambda}_i} \hat{\phi}_i(x)$, where $\hat{\lambda}_i$ and $\hat{\phi}_i(x)$ are eigenvalues and eigenfunctions, respectively, of the kernel K in Eq. (4) computed from the Fredholm integral equation [26]:

$$\int K(x, x') \hat{\phi}(x') dx' = \hat{\lambda} \hat{\phi}(x). \quad (5)$$

With this choice of basis set the expansions in Eq. (3) for the fields δ^k , δ^ξ and δ^η become Karhunen–Loeve (KL) expansion [26], such that ω_i^k , ω_i^ξ , and ω_i^η are uncorrelated random variables with zero means and unit variances.

Remarks. The Gaussian process and KL expansion are intentionally presented in Section 2.2.4 “Representation of problem-specific prior knowledge” to emphasize the fact that they are our specific choices for this problem and prior knowledge only. The optimal choice of basis set depends on the specific characteristics (e.g., smoothness, compactness of support) of the prior. Other functional basis sets including wavelets [27] or radial basis functions [28] will be explored in future works.

2.3. Inverse Modeling Based on an Iterative Ensemble Kalman Method

After the transformations above, the Reynolds stresses random field $\boldsymbol{\tau}(x)$ is parameterized by the coefficients ω_i^k , ω_i^ξ , and ω_i^η in Eq. (3), which are truncated to m modes and written in a stacked vector form as follows⁴:

$$\boldsymbol{\omega} \equiv [\omega_1^k, \omega_1^\xi, \omega_1^\eta, \omega_2^k, \omega_2^\xi, \omega_2^\eta, \dots, \omega_m^k, \omega_m^\xi, \omega_m^\eta] \quad (6)$$

We employ an *iterative, ensemble-based* Bayesian inference method [29] to combine the prior knowledge as represented above and the available data to infer the distribution of $\boldsymbol{\omega}$. This method is closely related to ensemble filtering methods (e.g., ensemble Kalman filtering), which are a class of standard data assimilation techniques used in numerical weather forecasting [30]. An overview of the ensemble Kalman-based inverse modeling procedure is presented in Fig. 2. In the iterative ensemble method, the state of the system \mathbf{x} is defined to include both the physical variables (i.e., velocity field \mathbf{u}) and the unknown coefficients $\boldsymbol{\omega}$, i.e., $\mathbf{x} \equiv [\mathbf{u}, \boldsymbol{\omega}]^T$. This is called “state augmentation” [29]. One starts with an ensemble of states $\{\mathbf{x}_j\}_{j=1}^N$ drawn from their prior distributions. During each iteration, all samples in the ensemble are updated to incorporate the observations through the following procedure:

1. reconstruction of Reynolds stresses from the coefficients $\boldsymbol{\omega}$,
2. computation of velocity fields from the given Reynolds stress fields by solving the RANS equations (implemented as forward model tauFoam, detailed in Section 3), and
3. a Kalman filtering procedure to assimilate the velocity observation data to the computed states, leading to an updated ensemble incorporating the observation data.

The updating procedure is repeated until the ensemble is statistically converged. The converged ensemble is considered a sample-based representation of the posterior distribution of the system state, from which the mean, variance, and higher moments can be computed. The algorithm of the inversion scheme is presented in Appendix B, and further details can be found in [29].

An important property of the iterative ensemble Kalman method is that the posterior ensembles and its mean all lie in the linear space \mathbf{X} spanned by the prior ensemble $\{\mathbf{x}_j\}_{j=1}^N$. In essence, this scheme attempts to search the space \mathbf{X} to find the optimal solution that minimizes the L2 norm of the misfit between the posterior mean and the observations, accounting for the uncertainties in both [29]. As with many inverse problems, this problem is

⁴It is trivial for each variable to have different number of modes, but this possibility is omitted here to simplify notation.

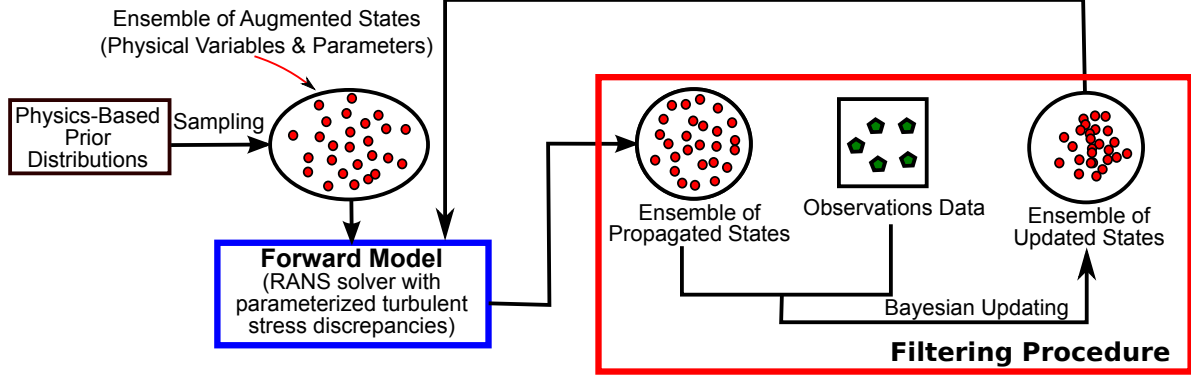


Figure 2: Inference of coefficients in the parameterized model discrepancies (e.g., discrepancies in RANS modeled Reynolds stresses) using an iterative ensemble Kalman inversion method. This approach combines prior knowledge of a given problem and available data to quantify and reduce model-form uncertainty.

intrinsically ill-posed. Specifically, because of the sparseness of the observation (the scenario of concern in our work), the amount of data is usually not sufficient to constrain the uncertainties in the states, which include the model discrepancy as components. The forward model essentially serves as regularization of the ill-posedness with its physical representation of the system dynamics.

The ensemble Kalman-based uncertainty quantification scheme used here is an approximate Bayesian method, and is computationally cheaper than the exact Bayesian scheme based on Markov Chain Monte Carlo sampling. It is not expected to give posterior distributions with comparable accuracy to those obtained from exact Bayesian schemes [31]. This will be further discussed in Section 5.

2.4. Summary of the Algorithm in the Proposed Framework

In summary, the overall algorithm of the proposed framework for quantifying and reducing uncertainties in a RANS simulation is presented in Algorithm 1.

3. Implementation and Numerical Methods

The uncertainty quantification framework including the mapping of Reynolds stresses and the iterative ensemble Kalman method is implemented as in-house codes in Python, which interfaces with RANS models and the KL expansion procedures to form the complete framework. The package UQTK developed by Sandia is used to perform the KL expansion [32]. Two types of RANS solvers are used in this framework, a conventional baseline

Algorithm 1 Model-form uncertainty quantification and reduction for RANS simulations

1. Perform the baseline RANS simulation to obtain the velocity $\tilde{\mathbf{u}}^{rans}(x)$ and Reynolds stress $\tilde{\boldsymbol{\tau}}^{rans}(x)$.
 2. Perform the transformation $\tilde{\boldsymbol{\tau}}^{rans} \mapsto (\tilde{k}^{rans}, \tilde{\xi}^{rans}, \tilde{\eta}^{rans})$.
 3. Compute KL expansion to obtain basis set $\{\phi_i(x)\}_{i=1}^m$, where m is the number of modes retained.
 4. Generate initial prior ensemble of coefficient vectors $\{\boldsymbol{\omega}_j\}_{j=1}^N$, where N is the ensemble size.
 5. Use iterative scheme shown in Fig. 2 to obtain the posterior ensemble of the state distribution. Specifically, in each iteration do the following:
 - (a) Recover the discrepancy fields δ^k , δ^ξ , and δ^η from the coefficient $\{\boldsymbol{\omega}_j\}_{j=1}^N$ in the current state and the basis functions via Eq. (3), and further to obtain realization of k , ξ , and η from Eq. (2) for each sample in the ensemble.
 - (b) Obtain Reynolds stress ensembles $\{\boldsymbol{\tau}_j\}_{j=1}^N$ via mapping $(k, \xi, \eta) \mapsto \boldsymbol{\tau}$.
 - (c) For each sample in the ensemble $\{\boldsymbol{\tau}_j\}_{j=1}^N$, solve the RANS equations for velocity field \mathbf{u}_j with given Reynolds stress field $\boldsymbol{\tau}_j$.
 - (d) Compare the ensemble mean with velocity observations, and use Kalman filtering procedure to correct the augmented system state ensemble $\{\mathbf{x}_j\}_{j=1}^N$, where $\mathbf{x}_j = [\mathbf{u}_j, \boldsymbol{\omega}_j]^T$. The updated coefficient vector ensemble $\boldsymbol{\omega}_j$ is thus obtained as part of the system state ensemble.
 - (e) Stop if statistical convergence of the ensemble is achieved.
-

RANS solver `simpleFoam` and a forward RANS solver `tauFoam` which computes velocity field with a given Reynolds stress field. Both solvers are described as below.

The baseline simulation uses a built-in RANS solver `simpleFoam` in OpenFOAM for incompressible, steady-state turbulent flow simulations. OpenFOAM (for “Open source Field Operation And Manipulation”) is an open-source, general-purpose CFD platform based on finite-volume discretization. The platform consists of a wide range of solvers and post-processing utilities. The SIMPLE (Semi-Implicit Method for Pressure Linked Equations) algorithm [33] is used to solve the coupled momentum and pressure equations. Collocated grids are used, and the Rhie and Chow interpolation is used to prevent the pressure–velocity decoupling [34]. Second-order spatial discretization schemes are used to solve the equations on an unstructured, body-fitting mesh. Given the specification of the flow including initial conditions (to start the iteration), boundary conditions, geometry, and the choice of turbulence model, the `simpleFoam` solver computes the velocity field along with Reynolds stresses by solving the RANS equations as well as the equations for the turbulence quantities (e.g., turbulent kinetic energy k and the rate of dissipation ε for k – ε models). We choose the Launder–Sharma low Reynolds number k – ε model [35] in the baseline simulations, since uncertainties are injected to Reynolds stress field by modeling $\boldsymbol{\tau}$ as a random field. Accordingly, the meshes are refined wall-normal direction near the wall to resolve the boundary layer. This is to avoid the complexity of using wall-functions, which is in consistent with the work of Emory et al. [18]. As can be seen in the overall algorithm 1, for each uncertainty quantification case the baseline simulation is performed only once.

The forward RANS model `tauFoam` is invoked repeatedly in the Bayesian inference procedure. This solver is adopted from and similar to `simpleFoam` except that it computes the velocity directly with a *given Reynolds stress field*. There is no need to specify a turbulence model and or to solve the equations for turbulence quantities, since the Reynolds stress is given. Hence, its computational cost for each call of the forward RANS model `tauFoam` is slightly lower than that of the conventional RANS solver `simpleFoam`.

4. Numerical Simulations

Two canonical flows, the flow in a channel with periodic constrictions (periodic hills) and the fully developed turbulent flow in a square duct, are chosen to evaluate the performance of the proposed framework. The periodic hill flow features a recirculation zone formed by a forced separation, a strong mean flow curvature due to the domain geometry, and a shear layer that is not aligned with the overall flow direction. All these features are known to pose

challenge for turbulence modeling. The square duct flow is characterized by a secondary flow pattern in the plane perpendicular to the main flow. The in-plane secondary flow is driven by the imbalance in the normal components of the Reynolds stress tensor, which cannot be captured by models with isotropic eddy viscosity turbulent models including most of the widely used models such as $k-\varepsilon$, $k-\omega$, and Spalart–Allmaras models. The two challenging cases are chosen to demonstrate the capability of the proposed framework in quantifying and reducing uncertainties in the RANS model predictions by incorporating sparse observations.

4.1. Flow over Periodic Hills

4.1.1. Case setup

The periodic hill flow is widely used in the CFD community to evaluate performance of turbulence models due to the availability of experimental and numerical benchmark data [36]. The geometry of the computational domain and the coordinate system are shown in Fig. 3. The Reynolds number based on the crest height H and the bulk flow velocity U_b at the crest is $Re_b = 2800$. Periodic boundary conditions are applied in the streamwise (x) direction, and non-slip boundary conditions are applied at the walls. The flow is two-dimensional, and thus the spanwise (z) direction is not considered.

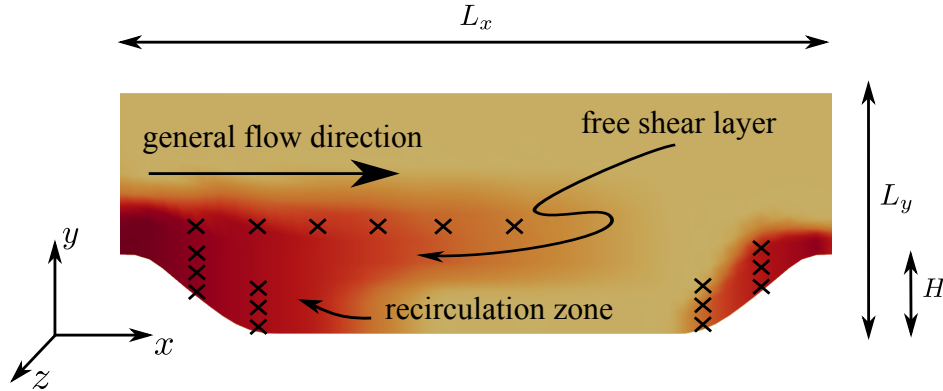


Figure 3: Domain shape for the flow over periodic hills. The x -, y - and z -coordinates are aligned with streamwise, wall-normal and spanwise directions, respectively. All dimensions are normalized with H with $L_x/H = 9$, $L_y/H = 3.036$. The contour shows the variance field $\sigma(x)$, where darker color represents the larger variance. The locations where velocities are observed are indicated as crosses (\times).

The mesh and computational parameters used in the uncertainty quantification procedure are presented in Table 1. The uncertainties in ξ , η , k are all considered, and thus δ^ξ ,

δ^η and δ^k are all random fields. This choice is based on our prior knowledge that both the Reynolds stress anisotropy (indicated by the shape τ , or equivalently, ξ and η) and turbulent kinetic energy k predicted by the RANS model are biased, and both are important for the accurate prediction of the flow behavior. The length scale parameter l is chosen according to the approximate length scale of the flow, which can be obtained either from our physical understanding of the flow or, if that is not available, from the baseline RANS simulation. Velocity observations are generated by adding Gaussian random noises with standard deviation σ_{obs} to the truth from DNS data. The noises at different locations are uncorrelated. The observation points are arranged so that they are closer in regions where the spatial changes of the flow are more rapid (the recirculation zone leeward of the hill and the reattached flow region windward of the hill), and are further apart in the free shear region downstream of the hill crest. This arrangement of observations is expected in actual experiments. The ensemble usually converges in approximately 30 iterations.

The non-stationary Gaussian process models for δ^ξ , δ^η and δ^k share the same variance field $\sigma(x)$, which are shown as flood contour in Fig. 3. Design of the variance field is strictly based on physical prior knowledge as described in Section 2.2.4, and does not take the DNS data into account, since the complete field of the true Reynolds stresses are rarely known in practical applications. Parameter sensitivity analysis has been conducted to ensure that reasonable variations of the computational parameters above (including the variance field design) do not lead to significantly different results or conclusions. In particular, when constant variance field $\sigma(x)$ is used (corresponding to the lack of problem-specific prior knowledge), the results do deteriorate as expected, but are still in acceptable range.

4.1.2. Results

The first six modes of the KL expansion are presented in Fig. 4, along with two typical realizations. This is to illustrate the uncertainty space of the Reynolds stress discrepancy field (or more precisely its projections δ^ξ , δ^η and δ^k) . All the modes have been shifted and normalized to the range $[0, 1]$. It can be seen that in all the models and the realizations the variations mostly concentrate in the three pre-specified regions (recirculation zone, free shear region, and the reattached flow windward of the hill), and the upper part of the channel has rather small variations. This is consistent with our physical prior knowledge specified through the variance field design.

Accurate predictions of the recirculation and the reattachment of the flow are of the most interest in the flow over periodic hills. Therefore, we identify three QoIs for this case: (1) the velocity field, in particular the velocities in the recirculation zone and reattached flow

Table 1: Mesh and computational parameters used in the flow over periodic hills and the flow in a square duct.

cases	periodic hill	square duct
mesh ($n_x \times n_y$)	50×30	30×30
number of samples N	60	
fields with uncertainty	ξ, η, k	ξ, η
number of modes m per field	16	8
length scale ^(a)	1	0.1
number of observation	18	$26^{(b)}$
standard deviation of observation noise (σ_{obs})	10% of truth	

(a) normalized by hill crest height H and domain size h for the periodic hill case and square duct case, respectively.

(b) Only 13 points of velocity data are supplied effectively due to the diagonal symmetry.

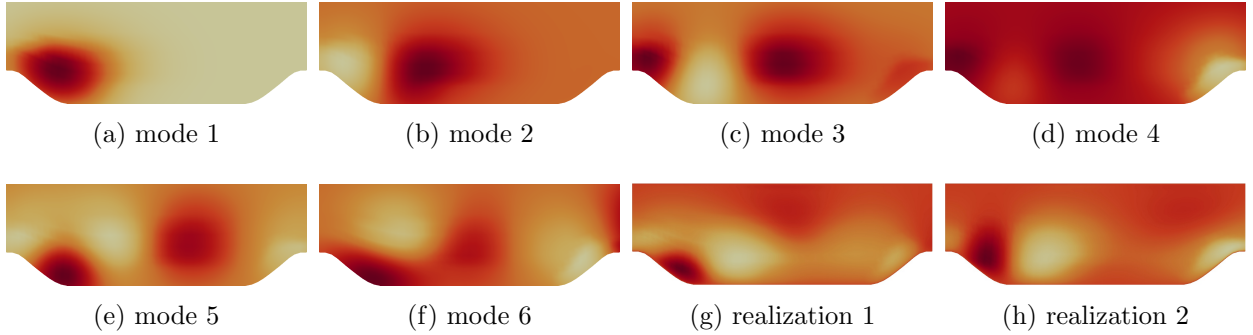


Figure 4: Illustration of KL expansion modes of the periodic hill case. All the modes have been shifted and scaled into the range between 0 (lightest) and 1 (darkest) to facilitate presentation, and the legend is thus omitted. Panels (a) to (f) represent modes 1 to 6, respectively. Lower modes are more important. Panels (g) and (h) show the turbulent kinetic energy associated with two typical realizations of the Reynolds stress discrepancy fields.

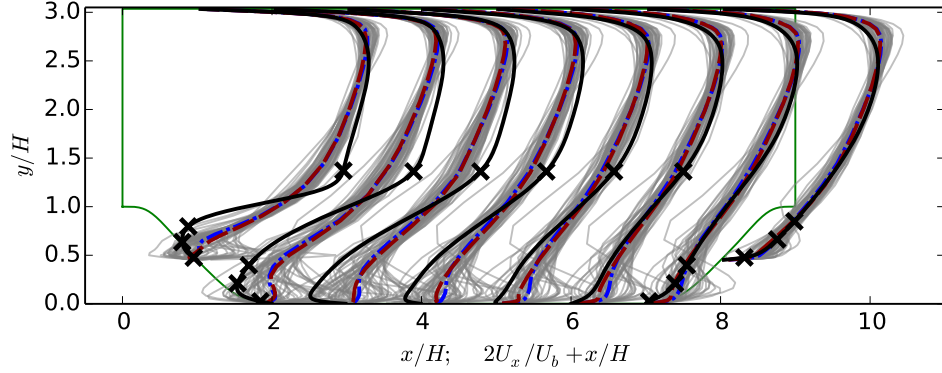
region windward of the hill, (2) the distribution of shear stresses τ_w on the bottom wall, and (3) the reattachment point x_{attach} . Other quantities that are important in engineering design and analysis (e.g., friction drag, form drag, size of separation bubble) are closely related to the three QoIs above.

The prior and posterior ensembles of the velocities are presented in Fig. 5 with comparison to the DNS benchmark results. The geometry of the domain is also shown to facilitate visualization. From Fig. 5a it can be seen that the prior mean velocity profiles are very close to those from the baseline RANS simulation, with only minor differences at a few locations (e.g., near the bottom wall at $x/H = 4, 5$, and 6). This is not surprising, since the Reynolds stresses prior ensemble use the RANS modeled Reynolds stress $\tilde{\boldsymbol{\tau}}^{rans}$ as the mean. In other words, the ensemble is obtained by introducing perturbations to the $\tilde{\boldsymbol{\tau}}^{rans}$. Therefore, the similarity between the velocity profiles in the baseline simulation and those of the prior ensemble indicates that the mapping from Reynolds stress to velocity is approximately linear with respect to the perturbations introduced to the prior Reynolds stresses ensemble. Clearly, both the baseline velocities and the prior mean velocities deviate significantly from the benchmark results, particularly in the recirculation region (leeward of the hill). From Fig. 5 it can be seen that the posterior ensemble mean of the velocities along all the lines are significantly improved compared to the baseline results. The remaining difference between the posterior mean of the velocity and the benchmark data is expected, since the posterior mean Reynolds stress must reside in the space \mathbf{X} spanned by the prior ensemble, and there is no guarantee that the true Reynolds stress is in this space.

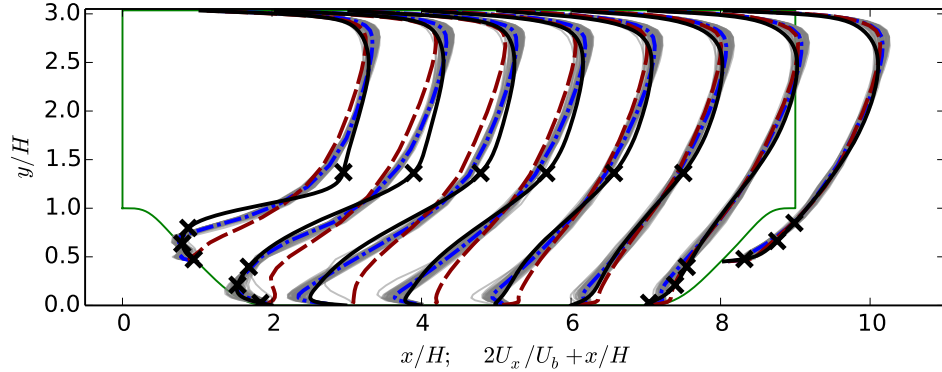
There are two reasons that can contribute to the fact that space \mathbf{X} may not contain the true Reynolds stress. First, uncertainties are only introduced to the magnitude (k) and shape (ξ and η) of the baseline Reynolds stresses, and not to the orientations (\mathbf{v}_1 , \mathbf{v}_2 , and \mathbf{v}_3). Second, a limited number of modes are retained in the KL expansion, which correspond to very smooth fields of Reynolds stress discrepancies. Therefore, if we think of the true Reynolds stress as residing in a high-dimensional space, in the current framework we assume that the truth is reasonably close to the baseline prediction $\tilde{\boldsymbol{\tau}}^{rans}$, and thus we only search the vicinity of $\tilde{\boldsymbol{\tau}}^{rans}$ for realizable candidates. This is justified by the confidence that the chosen baseline RANS model is rather capable, usually backed by enormous previous experiences in the community on the model of concern.

Finally, we emphasize that if the true Reynolds stresses did reside in the space spanned by the prior ensemble, the posterior mean velocity would indeed coincide with the true velocity. This scenario could occur if the baseline Reynolds stress $\tilde{\boldsymbol{\tau}}^{rans}$ only differs from the true

Reynolds stress in magnitude k and shape ξ and η , and the discrepancy is smooth enough to be represented by the chosen number of modes. However, both scenarios are rather unlikely in any nontrivial cases. For verification purposes we have designed a case of flow over periodic hills with synthetic data (as opposed to DNS data) that satisfies the requirements above, and have confirmed that the obtained posterior mean velocity indeed exactly agree with the truth in this case. The results are omitted here for brevity.



(a) Prior velocities ensemble



(b) Posterior velocities ensemble

— samples - - - sample mean - - - baseline
— DNS × × observations

Figure 5: The prior and posterior ensembles of velocity profile for the flow over periodic hill at eight locations $x/H = 1, \dots, 8$ compared with benchmark data and baseline results. The locations where velocities are observed are indicated with \times .

The other two QoIs, bottom wall shear stress τ_w and the reattachment point x_{attach} , are shown in Fig. 6. Similar to the velocity profiles in Fig. 5, both prior and posterior ensembles are presented and compared with benchmark data and baseline results. It can be seen from

Fig. 6a that the prior ensemble means of both τ_w and x_{attach} deviate from the benchmark DNS data significantly. In particular, the baseline RANS simulation predicts a much smaller recirculation zone than the truth. Figure 6b shows that in most part of the region (between $x/H = 1$ and $x/H = 8$) the posterior ensemble mean has better agreement with the DNS data than the baseline results. In fact, in this region all samples in the posterior ensemble has better agreement with the benchmark than the baseline results in terms of both wall shear stress and reattachment point. This improvement demonstrates the merits of the current framework. Incorporating observation data and physical prior knowledge indeed leads to improved predictions of both QoIs studied here.

It is noted that in the immediate vicinity of the hill crest, i.e., near $x/H = 0.5$ and $x/H = 8.5$, the posterior ensemble is similar to or even slightly deteriorated compared to the baseline in terms of agreement with DNS data. The reason is that in this region the flow has rapid spatial variations. Specifically, there is a separation between $0 < x/H < 1$, and a large mean flow curvature with strong pressure gradient between $8 < x/H < 9$. Consequently, the length scale of the flow field in this region is small, and thus the correlations between this part of the flow and other regions are weak. On the other hand, no velocity observations are available in this region. Here we point out an important fact that the Bayesian inference based on ensemble Kalman method primarily relies on the *correlation* between the predicted system state variables at different locations to make corrections. Specifically, the observations only bring information to the states at the locations correlated to the observed states. Hence, poor prediction is expected for a region that has neither observations within it nor statistically significant correlations with the regions that have observations.

The correlation structure (e.g., of the velocities) in a flow field is very complex and difficult to visualize due to the high dimensionality of the state. However, we can illustrate the idea by considering the streamlines of the mean flow. Intuitively, velocities at two points on the same streamline should have a relatively high correlation. Consequently, observing the velocity at one point can inform us about velocities at other points on the same streamline. Two points in different coherent structures or regions as mentioned above, e.g., one point in the recirculation zone and another in the shear zone, are likely to be on different streamlines. This explains why points within the same region have higher correlations than the correlations among different regions. That also justifies the arrangement of observation points shown in Fig. 3 with observations scattered in all three regions of interest. This explanation of correlation structure is of course a highly simplified picture. In reality, fluid flows are highly complex, coupled dynamic systems described by the RANS equations. Velocities at different

points can be correlated due to continuity requirements and pressure. It is well known that the pressure is described by an elliptic equation (for incompressible flows), which has whole-domain coupling characteristics.

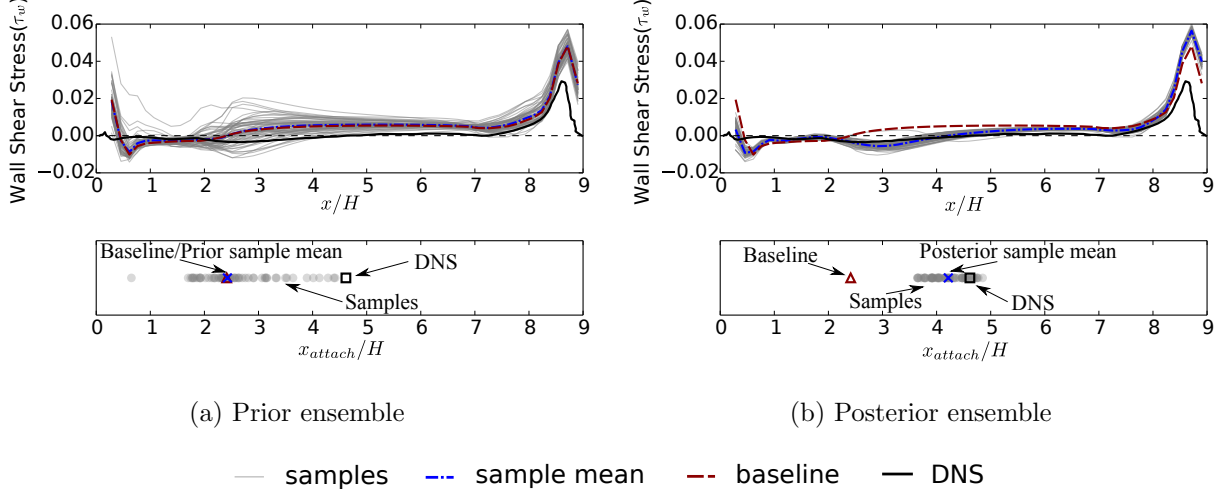


Figure 6: (a) Prior ensemble and (b) posterior ensemble of the bottom wall shear stress τ_w (*top panels*) and reattachment point x_{attach} (*bottom panels*) for the flow over periodic hills. The region with negative shear stress τ_w indicates the extent of recirculation zone on the bottom wall. The reattachment point is the downstream end of the recirculation zone, and can be determined by the location at which the wall shear stress changes from negative to positive. Note that certain samples in the ensemble have two recirculation zones that are very close to each other. In these cases the reattachment point of the downstream one is taken.

The prior and posterior distributions of the reattachment point represented by probability density functions (PDF) are shown in Fig. 7. It can be seen in Fig. 7a that the biases in prior distribution as compared to the DNS data is large. In addition, the PDF of the prior distribution is wide, indicating the lack of information. Figure 7b shows that in the posterior distribution the bias compared to the DNS data is significantly corrected. Moreover, the support of posterior distribution is narrowed, which indicates increase of confidence upon the prediction due to the incorporation of information from the velocity observations in the Bayesian inference.

Figure 8 shows that the bias in the turbulent kinetic energy (TKE) from baseline RANS prediction has been partly corrected, especially for the upstream region. It is possible that the production of TKE due to the instability in the free-shear region after the separation

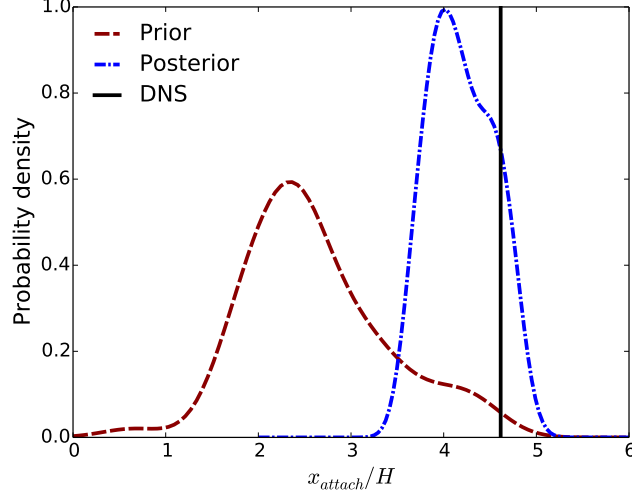


Figure 7: Probability density functions of the prior and posterior distribution of the reattachment point x_{attach} . Gaussian kernel function with bandwidth 1 is used to obtain the smooth probability density curve from the histogram of samples. The area below the probability density curve is one due to the normalization requirement.

is the driven factor. Consequently, the improved prediction of TKE in this region leads to the corrections for the velocities and other QoIs in the entire field. However, note that the posterior mean of TKE is not necessarily better than the baseline results at all locations. The TKE level in immediate downstream of the hill crest has been increased, but at the downstream locations the posterior mean are not significantly better than the baseline. In the process of minimizing misfit with the observations, some compromises are inevitably made, with some regions having corrections (e.g., the upstream region) than others (the downstream region). A possible explanation is that the TKE in the free-shear region has stronger correlations with the velocities at the observed locations.

4.2. Fully Developed Turbulent Flow in a Square Duct

4.2.1. Case setup

The fully developed turbulent flow in a square duct is a widely known case for which many turbulence models fail to predict the secondary flow induced by the Reynolds stresses. The geometry of the case is shown in Fig. 9. The Reynolds number based on the edge length D of the square and the mean friction velocity U_τ is $Re_\tau = 600$. All lengths presented below are normalized by the height h of the computational domain, which is a half of D . Extensive benchmark data from DNS are available in the literature [37, 38].

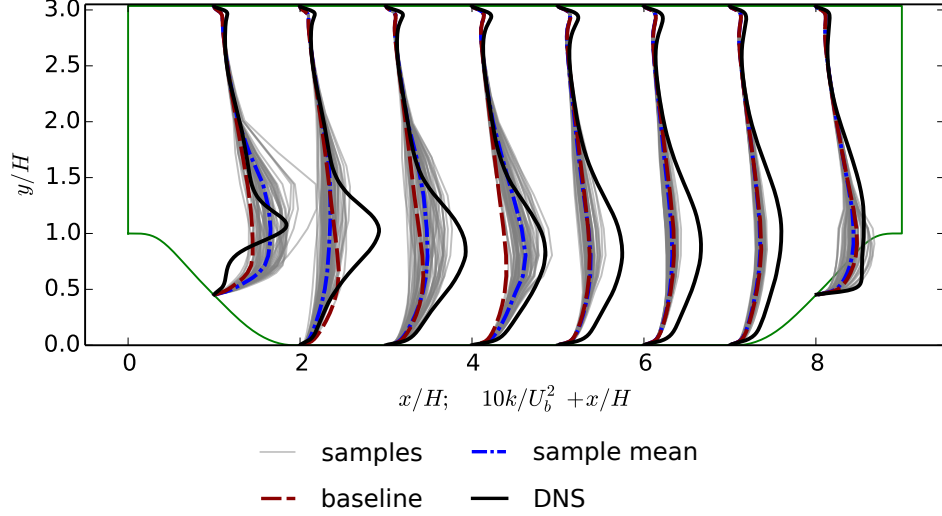


Figure 8: Posterior ensemble of the turbulent kinetic energy k with its mean compared to the baseline results and the benchmark DNS data. The prior ensemble is omitted for k , since its mean is the same as the baseline prediction.

Standard computational setup as used in the literature is adopted in this work. Only one quadrant of the physical domain is simulated considering the symmetry of the flow with respect to the centerlines along y - and z -axis as indicated in Fig. 9. We emphasize here that our study is concerned with the mean flow, since the objective is to quantify the uncertainties in RANS simulations. The instantaneous flows are beyond the scope of our discussions, and they do not have the symmetries mentioned here. Non-slip boundary conditions are imposed at the walls and symmetry boundary conditions (zero in-plane velocities) are applied on the symmetry planes. Theoretically, one can further reduce the computational domain size to 1/8 of the physical domain by utilizing the symmetry with respect to the square diagonal. However, this symmetry is not exploited, as it would be difficult to impose proper boundary conditions on the diagonal. The symmetry in the baseline RANS simulation results is implied by the diagonal symmetry of the geometry and boundary conditions. When conducting forward RANS simulations with given Reynolds stress fields, caution must be exercised to ensure that the perturbations introduced to $\tilde{\tau}^{rans}$ have diagonal symmetry, which will be discussed later.

The mesh and computational parameters for this case are shown in Table 1. Choice of parameters can be motivated similarly as in the periodic hill case. A notable difference is that only uncertainties in the shape of the Reynolds stress (i.e., ξ and η) are considered in the square duct flow case. The QoI for this flow is the in-plane flow velocities, which are

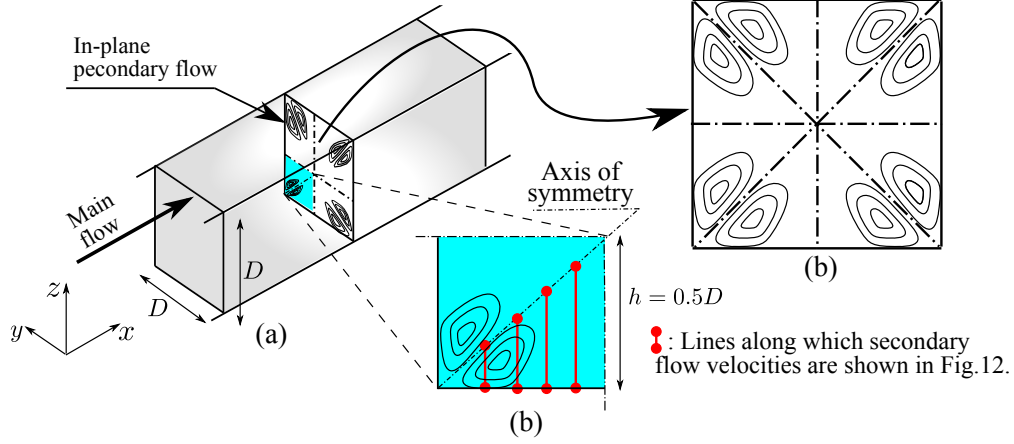


Figure 9: (a) Schematic for the fully developed turbulent flow in a square duct. The x axis is aligned with the streamwise direction. Secondary flows exist in the y - z plane, which are schematically represented with contours. (b) Symmetry of the (mean) flow with respect to the centerlines in y - and z -directions and along the diagonals. (c) The computational domain covers only a quarter of the physical domain due to the centerline symmetry. The cross-sections along which QoIs (e.g., velocities and Reynolds stress imbalance) are compared to benchmark data are also indicated.

primarily driven by the normal stress imbalance $\tau_{yy} - \tau_{zz}$, a quantity that is associated with the shape of $\boldsymbol{\tau}$. The design of the variance field σ is based on the same principle as in the periodic hill flow. It is known that RANS models have more difficulties in predicting the flow near the corner, which justifies the large value of $\sigma(x)$ near the corner and the gradual decrease away from the corner as well as towards the diagonal. Moreover, the variance field is chosen to be symmetric along the diagonal of the y - z plane in consideration of the flow symmetry.

4.2.2. Results

The first six modes of KL expansion are shown in Fig. 11 along with two typical realizations. All the modes have been shifted and normalized into the range $[0, 1]$. Only the diagonally symmetric modes are retained to guarantee the symmetry of the Reynolds stress along the diagonal, which leads to the symmetry of the posterior velocities. The observations are obtained from the DNS data [37] by adding Gaussian random noises as in the periodic hill flow. Velocities are observed at 26 points as shown in Fig 9, half of which are distributed along the line $y/h = 0.5$ and the other half along $z/h = 0.5$. Note that half of the information from the observations is redundant due to the diagonal symmetry of the flow.

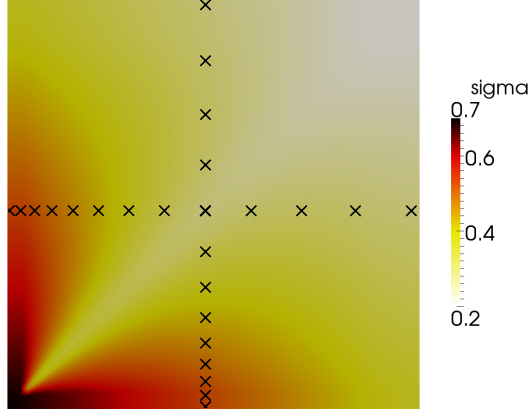


Figure 10: Contour of the variance field $\sigma(x)$ and locations of the observations for the square duct flow case. Larger variances are allowed near the corner due to the difficulties RANS models have in predicting the secondary flow in this region. The variance field is chosen to be symmetric along the diagonal of the y - z plane in consideration of the flow symmetry.

The ability of a numerical model to predict the secondary flow in y - z plane is of most interest for the flow in square duct. Therefore, the in-plane velocity field is identified as the QoI for this case. The in-plane flow velocity (U_y) on the four cross-sections as indicated in Fig. 9 are presented to facilitate quantitative comparison with the baseline and benchmark results. The velocity profiles U_z in the z direction have similar characteristics as U_y (but are not identical) and are thus omitted. The prior and posterior ensembles of the velocity profiles for U_y are shown in Fig. 12. Only the velocity profiles in the region below the diagonal are presented due to the diagonal symmetry. It can be seen from Fig. 12 that the baseline RANS simulation predicts uniformly zero in-plane velocities as expected. Around the baseline prediction, the prior ensembles are scattered due to the perturbation of δ_ξ and δ_η . The large range of scattering indicates that the secondary flow is sensitive to the anisotropy of Reynolds stresses tensor, which has been reported in previous studies [19, 37]. Compared to the prior ensemble mean and the baseline RANS prediction, the posterior ensemble mean of the velocities are significantly improved along all four cross sections, as shown by good agreements with the benchmark data. The scattering has been significantly reduced as well, while still covering the truth adequately in most regions. The remaining differences and the regions where the ensemble fails to cover the truth can be explained similarly as in the periodic hill case.

Figure 13 shows a comparison of the posterior ensemble mean field of the in-plane flow velocity and the benchmark data. They are presented as quiver plots to show the overall

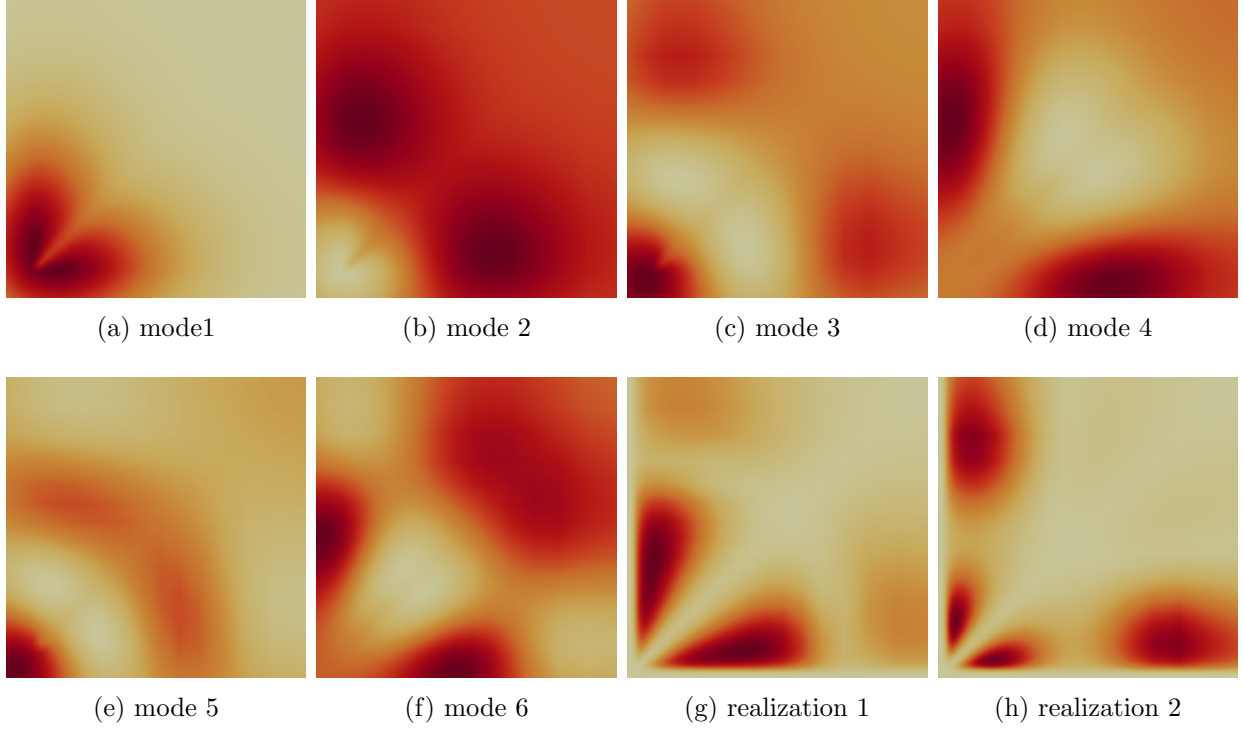


Figure 11: Illustration of KL expansion modes for the square duct flow case. All presented modes have been shifted and scaled into a range of 0 (lightest) to 1 (darkest) to facilitate presentation, and the legend is thus omitted. Panels (a) to (f) denote modes 1 to 6, respectively, with lower modes being more important. Only the modes with diagonal symmetry are retained to guarantee the symmetry of perturbed Reynolds stresses field. Panels (g) and (h) show the magnitude of Reynolds stress imbalance $|\tau_{yy} - \tau_{zz}|$ associated with two typical realizations of the discrepancy fields.

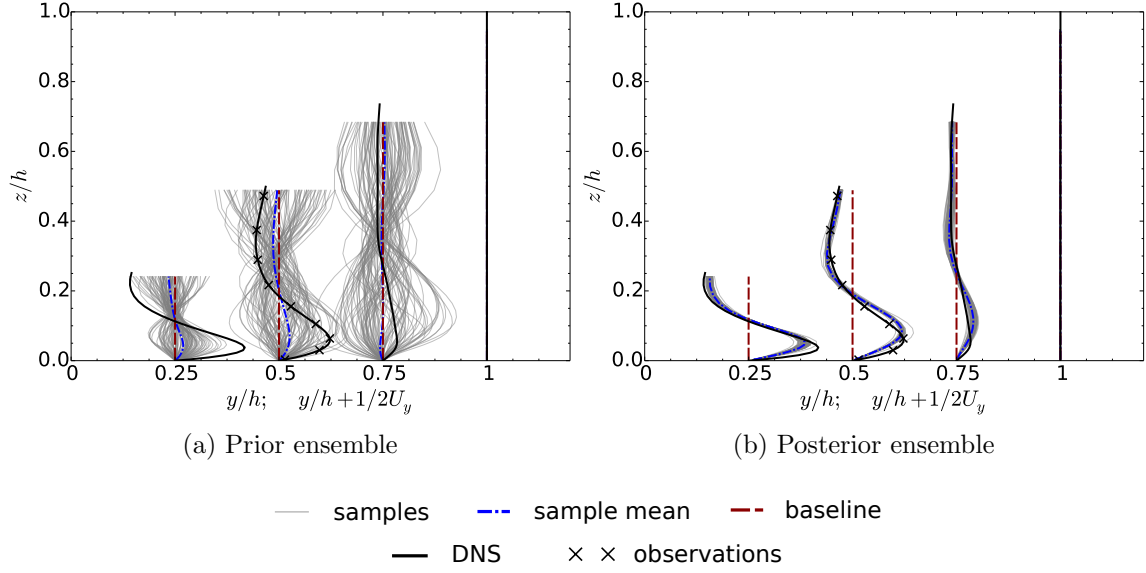


Figure 12: (a) Prior velocity ensemble and (b) posterior velocity ensemble at four spanwise locations $y/h = 0.25, 0.5, 0.75$ and 1 with comparison to baseline and benchmark results. The velocity U_z in the z direction have similar characteristics and are thus omitted. The velocity profiles in the prior ensemble are scaled by a factor of 0.3 for clarity.

features of secondary the flow and particularly the vortex structure. The length and direction of an arrow indicate the magnitude and direction, respectively, of the in-plane flow velocity at that location. The plots are arranged such that a perfect agreement between the two would show as exact symmetry of the two panels along the center line. The quiver plot of the velocity field from the baseline RANS prediction is omitted since it is uniformly zero. It can be seen that the posterior ensemble mean demonstrates a very good agreement with the benchmark data in most aspects, i.e., the direction and the intensity of secondary flow at most locations as well as the center of vortex structure. Only minor differences between the two can be identified. For example, the posterior mean velocity has a slightly smaller gradient of velocity magnitude compared to the benchmark results near the symmetry line. The agreement clearly demonstrates the merits of the current framework, particularly considering the fact that most of the commonly used turbulence models are not capable of predicting the in-plane flow. Specifically, all isotropic eddy viscosity models completely miss the secondary flow by construction, which is explained by the negligible $\partial U_y / \partial y$ and $\partial U_z / \partial z$ terms and the intrinsic assumption that that Reynolds stress is proportional to local strain rate of the mean flow. Even advance models (e.g., Reynolds stress transport models)

tend to underestimate the flow intensity [39]. Admittedly, velocity observations at some locations are used in this method, but the amount of data used in the inference is rather small compared to the total degree of freedom of the Reynolds stress field.

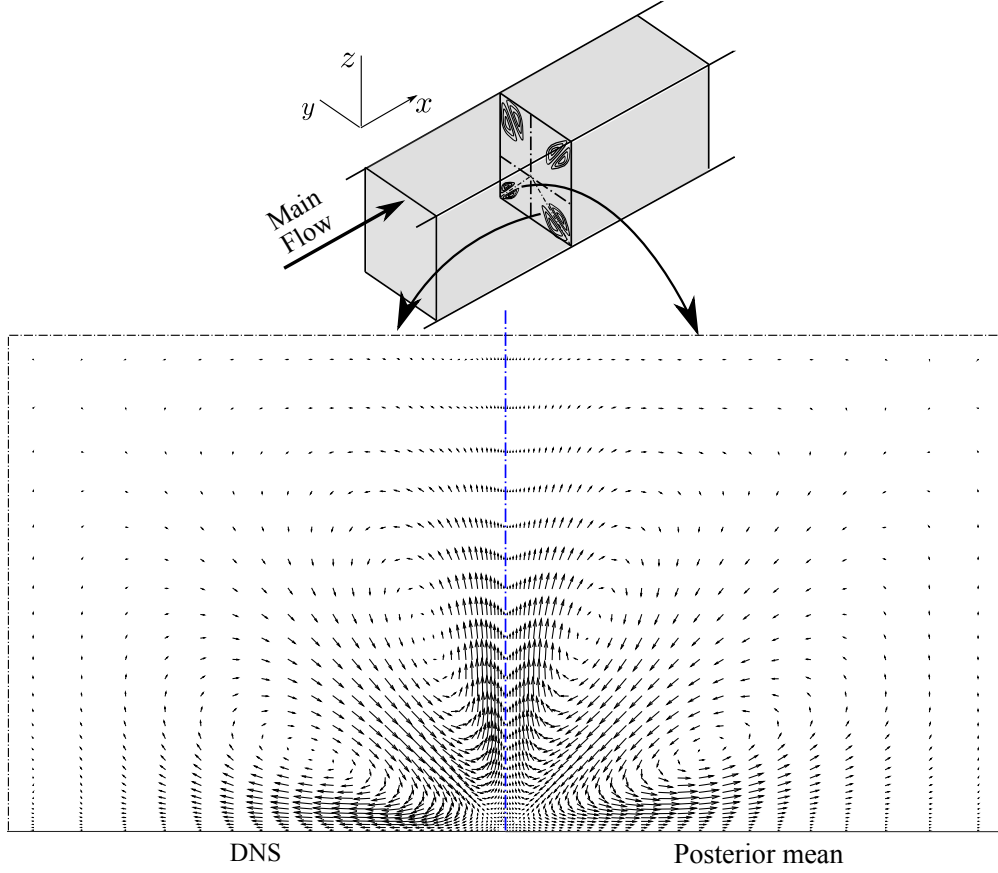


Figure 13: Comparison of velocity field of the flow in a square duct between the posterior mean and benchmark DNS data. The length and direction of an arrow indicate the magnitude and direction, respectively, of the in-plane flow velocity. The plots are arranged such that a perfect agreement between the two would show as exact symmetry of the two panels along the center line. The vector field of baseline RANS prediction is omitted since it is uniformly zero.

As mentioned above, the normal stress imbalance $\tau_{yy} - \tau_{zz}$ is the main driving force of the secondary flow. Therefore, the prior and posterior ensembles of the imbalance at five locations, $y/h = 0.25, 0.5, 0.6, 0.75$, and 1 , are presented in Fig. 14. It can be seen that the baseline RANS prediction of $\tau_{yy} - \tau_{zz}$ is zero. Compared to the baseline RANS prediction, the posterior normal stress imbalance shows a significant improvement in regions close to the observations ($y/h = 0.5$), although differences still exist, especially in the regions

far away from the observations (e.g., at $y/h = 1$). It is consistent with the argument made in Section 2.2.4 that the correlation decrease with distances, and that the quality of correction heavily depends on correlations. Note that the inferred stress imbalances at $y/h = 0.75$ agree with the benchmark much better than do those at $y/h = 0.25$, although they have approximately the same distances from the observations, which are distributed along $y/h = 0.5$. This can be explained by the fact that the length scale of the flow decreases towards the corner (e.g., near $y/h = 0.25$) due to the constriction of the duct walls, and thus the correlation decreases much faster in this region than near the symmetry line.

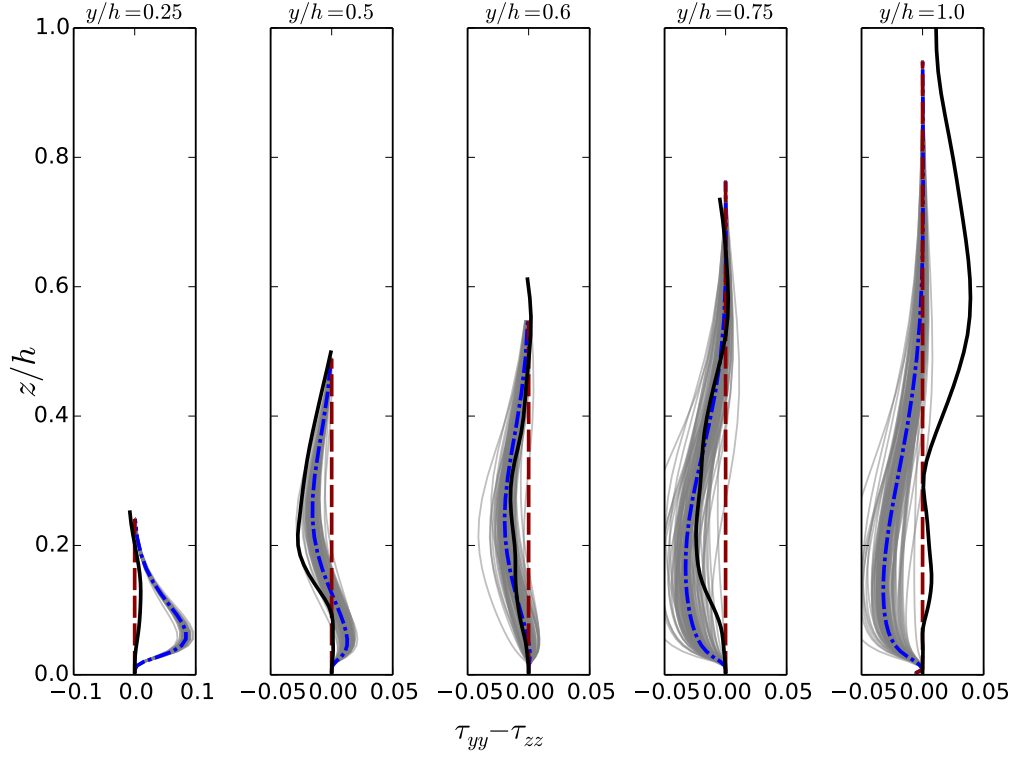


Figure 14: Comparison of normal stresses imbalance at five locations $y/h = 0.25, 0.5, 0.6, 0.75$ and 1.0 . A larger horizontal axis range is used in the panel for $y/h = 0.25$ due the large range of values $\tau_{yy} - \tau_{zz}$ at this location.

5. Discussion

5.1. Success and Limitation of the Current Framework

The overall idea of the proposed method is to improve velocity predictions and to quantify the uncertainties therein by combining all sources of available information, including observation data, physical prior knowledge, and RANS model predictions. A Bayesian framework

based on iterative ensemble Kalman method is used for the uncertainty quantification. Numerical simulation results have demonstrated the feasibility of the framework. In particular, even with velocity observations at very few locations, the posterior velocities are significantly improved compared to the baseline results.

One may also expect that the uncertainties in the modeled Reynolds stresses can be quantified and reduced. Indeed, the posterior ensemble obtained from the Bayesian inference process also has information of the Reynolds stresses. However, our experiences suggest that the posterior mean of an arbitrarily chosen component or projection of the Reynolds stresses is not significantly more accurate than those of the baseline prediction.

This apparent contradiction can be explained from the two perspectives, the high dimensionality of the Reynolds stress field and the mapping $\boldsymbol{\tau} \mapsto \mathbf{u}$ from Reynolds stresses to mean velocities. The most straightforward reason as mentioned in Section 2.3 is that the Reynolds stress discrepancy is a tensor field in a high-dimensional uncertainty space, and thus the amount of velocity data is not sufficient to constrain its uncertainties, even when other prior information is considered. Moreover, the RANS equations describe a many-to-one mapping from Reynolds stresses to mean velocities, and thus the mapping $\boldsymbol{\tau} \mapsto \mathbf{u}$ is not invertible (i.e., a given velocity field may correspond to many possible Reynolds stress fields). This is evident from the fact that the divergence of the Reynolds stress tensor, rather than the Reynolds stress itself, appears in the RANS equation. Although difficult to prove rigorously, we postulate that even Reynolds stress fields that have different divergences can map to very similar velocity fields. One can loosely think of the velocity field as being driven by certain *projection* of the Reynolds stress on a *low-dimensional manifold*. The specific form of the projection depends on the physics of individual flows. Taking the flow in square duct for example, it has been demonstrated by analytical derivations [19, 37, 40] that the secondary flow is primarily generated by the normal stress imbalance field $\tau_{yy} - \tau_{zz}$, or more precisely, its cross spatial derivative $\frac{\partial^2}{\partial y \partial z}(\tau_{yy} - \tau_{zz})$. The imbalance scalar can be obtained from the Reynolds tensor through linear mapping described by a rank deficient matrix. Since only velocity observation data are used in the Bayesian inference in this work, one can only reasonably expect to infer the projection (i.e., the imbalance), and not the full Reynolds stress field. This can be partly explained by the fact that the projection has a lower dimension, but more importantly, the projection is an observable variable from a control-theoretic perspective. This has been demonstrated in Fig. 14. The mapping between Reynolds stresses and velocity as describe by the RANS equations are extremely complex due to the their nonlinearity. This complexity and its implications to the current framework will be further

investigated.

Another limitation of the current framework lies in the iterative ensemble method used for the uncertainty quantification, which is a computationally affordable method for approximate Bayesian inference. The posterior distribution obtained with this method may deviate from the true distribution. This compromise is made in this work in consideration of the high computational costs of RANS models (e.g., hours to days for realistic flow simulations), which makes more accurate sampling methods such as those based on Markov Chain Monte-Carlo method prohibitively expensive. The accuracy of the ensemble-based method will be assessed in future works by comparing current results with those obtained with MCMC, possibly by utilizing recently developed dimension-reduction methods (e.g., active subspace methods [41], likelihood informed dimension-reduction [42]) and sampling techniques (e.g., delayed rejection adaptive metropolis [43]), or by building surrogate models to facilitate the MCMC sampling.

5.2. What if There Are No Observation Data Available

In light of the limitations of the framework as described above, two legitimate follow-up questions can be raised. That is, given that the full Reynolds stress discrepancy field cannot be inferred accurately from the velocity observations, (1) what would the value of the framework be in engineering practice, and (2) how this framework can be used in scenarios where no observation data.

Regarding the first question, sparse observation data are often available for engineering structures that are in operation. For example, real-time monitoring sensors are often installed in wind farms, nuclear power plants, and many other important facilities and devices. For these cases, the current framework can provide a powerful method for combining information from the numerical models (often greatly simplified due to stringent positive lead-time requirement in predictions), observation data, and physical prior knowledge.

In scenarios where there are no observation data available as posed in the second question, the current framework can be used in two ways. First, with the absence of observation data the inference procedure essentially degenerates to forward uncertainty propagation, i.e., propagating the uncertainties in the form of physical prior knowledge on Reynolds stresses to uncertainties in quantities of interests (e.g., velocity, wall shear stresses, and reattachment point). This is somewhat similar to but more comprehensive than the framework of Iaccarino and co-workers [15–19], since the prior in our work covers an uncertainty space rather than only a few limit states. Second, when observation data are available in a geometrically similar case but perhaps at a lower Reynolds number (e.g., the downscaled model in a laboratory

experiment), the model uncertainties can first be quantified and reduced with the data available on the scaled model. After the calibration, the posterior Reynolds stress uncertainty distribution is extrapolated to the case of concern (e.g., the flow in a geometrically similar prototype at a higher Reynolds number) to make predictions. Dow and Wang [20] used a similar calibration–prediction procedure to predict flows in channels of different geometries by using Gaussian processes describing the eddy viscosity discrepancy. In both cases the calibration–prediction procedure is based on a crucial assumption that the calibration case and the prediction case share physically similar characteristics, despite the differences in specific flow conditions (e.g., Reynolds number or geometry). Ultimately, the validity of this assumption has to be a judgment of the modeler. In this scenario we are essentially using expert prior knowledge, numerical model, and the data from a different problem to make predictions for a case of concern where no data are available. The feasibility of the calibration–prediction method based on the current framework will be explored in future research.

6. Conclusion

In this work we propose an open-box, physics-informed Bayesian framework for quantifying and reducing model-form uncertainties in RANS simulations. Uncertainties are introduced directly to the Reynolds stresses and are represented with compact parameterization accounting for empirical prior knowledge and physical constraints (e.g., realizability, smoothness, and symmetry). An iterative ensemble Kalman method is used to incorporate the prior knowledge with available observation data in a Bayesian framework, and propagate the uncertainties to posterior distributions of the Reynolds stresses and other quantities of interest. Two representative cases, the flow over periodic hills and the flow in a square duct, have been used to demonstrate the feasibility and to evaluate the performance of the proposed framework. Simulation results suggest that even with very sparse observations, the obtained posterior mean velocities have significantly better agreement with the benchmark data compared to the baseline results. The methodology provides a general framework for combining information from physical prior knowledge, observation data, and low-fidelity numerical models (including RANS models and beyond) that are frequently used in engineering practices.

A notable limitation is that the full Reynolds stresses field inferred from this method are not accurate. This is attributed to the high dimension of the Reynolds stress uncertainty space, the sparseness of the velocity observation data, and the nonlinear, possibly even non-

unique mapping between the Reynolds stresses and velocities as described by the RANS equations. However, we argue that the inferred Reynolds stresses are still valuable despite this limitation, and that they can be extrapolated to cases with similar physical characteristics. Another limitation of the current framework lies in the iterative ensemble method used for the uncertainty quantification, which is computationally less intensive but less accurate than exact Bayesian inference based on Markov Chain Monte-Carlo sampling. The impact of the approximate Bayesian inference method will be investigated in future studies.

References

- [1] D. C. Wilcox, Turbulence modeling for CFD, 3rd Edition, DCW Industries, 2006.
- [2] S. B. Pope, Turbulent Flows, Cambridge University Press, Cambridge, 2000.
- [3] C. J. Roy, W. L. Oberkampf, A comprehensive framework for verification, validation, and uncertainty quantification in scientific computing, *Computer Methods in Applied Mechanics and Engineering* 200 (25) (2011) 2131–2144.
- [4] A. Saltelli, P. Stano, P. B. Stark, W. Becker, Climate models as economic guides: Scientific challenge or quixotic quest?, *Issues in Science and Technology* 31 (3).
- [5] M. C. Kennedy, A. O’Hagan, Bayesian calibration of computer models, *Journal of the Royal Statistical Society: Series B (Statistical Methodology)* 63 (3) (2001) 425–464.
- [6] Y. Xiong, W. Chen, D. Apley, X. Ding, A non-stationary covariance-based kriging method for metamodeling in engineering design, *International Journal for Numerical Methods in Engineering* 71 (6) (2007) 733–756.
- [7] D. Huang, T. Allen, W. Notz, R. Miller, Sequential kriging optimization using multiple-fidelity evaluations, *Structural and Multidisciplinary Optimization* 32 (5) (2006) 369–382.
- [8] S. Conti, J. P. Gosling, J. E. Oakley, A. O’Hagan, Gaussian process emulation of dynamic computer codes, *Biometrika* (2009) asp028.
- [9] D. Higdon, M. Kennedy, J. C. Cavendish, J. A. Cafo, R. D. Ryne, Combining field data and computer simulations for calibration and prediction, *SIAM Journal on Scientific Computing* 26 (2) (2004) 448–466.

- [10] J.-X. Wang, C. J. Roy, H. Xiao, A multi-model approach for uncertainty propagation and model calibration in CFD applications, Submitted to Computers and Fluids Also available at arxiv:1501.03189.
- [11] J. Brynjarsdóttir, A. O'Hagan, Learning about physical parameters: The importance of model discrepancy., Inverse Problems 30 (2014) 114007.
- [12] T. Oliver, R. Moser, Uncertainty quantification for RANS turbulence model predictions, in: APS Division of Fluid Dynamics Meeting Abstracts, Vol. 1, 2009.
- [13] T. A. Oliver, R. D. Moser, Bayesian uncertainty quantification applied to rans turbulence models, in: Journal of Physics: Conference Series, Vol. 318, IOP Publishing, 2011, p. 042032.
- [14] S. H. Cheung, T. A. Oliver, E. E. Prudencio, S. Prudhomme, R. D. Moser, Bayesian uncertainty analysis with applications to turbulence modeling, Reliability Engineering & System Safety 96 (9) (2011) 1137–1149.
- [15] C. Górlé, G. Iaccarino, A framework for epistemic uncertainty quantification of turbulent scalar flux models for Reynolds-averaged Navier-Stokes simulations, Physics of Fluids 25 (5) (2013) 055105.
- [16] C. Górlé, J. Larsson, M. Emory, G. Iaccarino, The deviation from parallel shear flow as an indicator of linear eddy-viscosity model inaccuracy, Physics of Fluids 26 (5) (2014) 051702.
- [17] M. Emory, J. Larsson, G. Iaccarino, Modeling of structural uncertainties in Reynolds-averaged Navier-Stokes closures, Physics of Fluids 25 (11) (2013) 110822.
- [18] M. Emory, R. Pecnik, G. Iaccarino, Modeling structural uncertainties in reynolds-averaged computations of shock/boundary layer interactions, AIAA paper 479 (2011) 1–16.
- [19] M. A. Emory, Estimating model-form uncertainty in reynolds-averaged Navier–Stokes closures, Ph.D. thesis, Stanford University (2014).
- [20] E. Dow, Q. Wang, Quantification of structural uncertainties in the k – ω turbulence model, in: 52nd AIAA/ASME/ASCE/AHS/ASC Structures, Structural Dynamics and Materials Conference, AIAA, Denver, Colorado, 2011, aIAA Paper, 2011-1762.

- [21] C. K. Wikle, R. F. Milliff, D. Nychka, L. M. Berliner, Spatiotemporal hierarchical bayesian modeling tropical ocean surface winds, *Journal of the American Statistical Association* 96 (454) (2001) 382–397.
- [22] L. M. Berliner, Physical-statistical modeling in geophysics, *Journal of Geophysical Research: Atmospheres* 108 (D24).
- [23] B. Launder, G. Reece, W. Rodi, Progress in development of a Reynolds-stress turbulence closure, *Journal of Fluid Mechanics* 68 (1975) 537–566.
- [24] H. Tennekes, J. L. Lumley, *A first course in turbulence*, MIT press, 1972.
- [25] S. Banerjee, R. Krahl, F. Durst, C. Zenger, Presentation of anisotropy properties of turbulence, invariants versus eigenvalue approaches, *Journal of Turbulence* 8 (32).
- [26] O. P. Le Maître, O. M. Knio, *Spectral methods for uncertainty quantification: with applications to computational fluid dynamics*, Springer, 2010.
- [27] I. Daubechies, Orthonormal bases of compactly supported wavelets, *Communications on pure and applied mathematics* 41 (7) (1988) 909–996.
- [28] M. D. Buhmann, *Radial basis functions: theory and implementations*, Cambridge university press, 2003.
- [29] M. A. Iglesias, K. J. Law, A. M. Stuart, Ensemble Kalman methods for inverse problems, *Inverse Problems* 29 (4) (2013) 045001.
- [30] G. Evensen, *Data assimilation: the ensemble Kalman filter*, Springer, 2009.
- [31] K. Law, A. Stuart, Evaluating data assimilation algorithms, *Monthly Weather Review* 140 (2012) 3757–3782.
- [32] C. S. Bert Deusschere, Khachik Sargsyan, *UQTK User Manual*, Sandia National Laboratories, Albuquerque, New Mexico 87185 and Livermore, California 94550, version 2.1 Edition (June 2014).
- [33] S. V. Patankar, D. B. Spalding, A calculation procedure for heat, mass and momentum transfer in three-dimensional parabolic flows, *International Journal of Heat and Mass Transfer* 15 (10) (1972) 1787–1806.

- [34] C. M. Rhie, W. L. Chow, A numerical study of the turbulent flow past an isolated airfoil with trailing edge separation, *AIAA* 21 (11) (1983) 1525–1532.
- [35] B. E. Launder, B. I. Sharma, Application of the energy dissipation model of turbulence to the calculation of flow near a spinning disc, *Letter of Heat Mass Transfer*, 1 (1974) 131–138.
- [36] M. Breuer, N. Peller, C. Rapp, M. Manhart, Flow over periodic hills—numerical and experimental study in a wide range of reynolds numbers, *Computers & Fluids* 38 (2) (2009) 433–457.
- [37] A. Huser, S. Biringen, Direct numerical simulation of turbulent flow in a square duct, *Journal of Fluid Mechanics* 257 (1993) 65–95.
- [38] AGARD, A selection of test cases for the validation of large-eddy simulations of turbulent flows, Tech. Rep. 345, AGARD Advisory Report (1998).
- [39] A. Demuren, W. Rodi, Calculation of turbulence-driven secondary motion in non-circular ducts, *Journal of Fluid Mechanics* 140 (1984) 189–222.
- [40] H. Perkins, The formation of streamwise vorticity in turbulent flow, *Journal of Fluid Mechanics* 44 (04) (1970) 721–740.
- [41] P. G. Constantine, E. Dow, Q. Wang, Active subspace methods in theory and practice: Applications to kriging surfaces, *SIAM Journal on Scientific Computing* 36 (4) (2014) A1500–A1524.
- [42] T. Cui, J. Martin, Y. M. Marzouk, A. Solonen, A. Spantini, Likelihood-informed dimension reduction for nonlinear inverse problems, *Inverse Problems* 30 (11) (2014) 114015.
- [43] H. Haario, M. Laine, A. Mira, E. Saksman, DRAM: efficient adaptive MCMC, *Statistics and Computing* 16 (4) (2006) 339–354.
- [44] C. Hua, An inverse transformation for quadrilateral isoparametric elements: analysis and application, *Finite elements in analysis and design* 7 (2) (1990) 159–166.

Appendix A. Mapping from Barycentric coordinate to natural coordinate

Following the work of Iaccarino et al., we introduce uncertainties (also referred to as perturbations) to the Reynolds stresses by perturbing its magnitude (the turbulent kinetic energy k) and the shape (the eigenvalues λ_1 and λ_2 of the anisotropy tensor) as shown in Eq. (1). The eigenvalues can be linearly transformed to the Barycentric coordinate (C_1, C_2, C_3) as follows [18, 25]:

$$C_1 = \lambda_1 - \lambda_2 \quad (\text{A.1a})$$

$$C_2 = 2(\lambda_2 - \lambda_3) \quad (\text{A.1b})$$

$$C_3 = 3\lambda_3 + 1 \quad (\text{A.1c})$$

where C_1 , C_2 , and C_3 indicate the portion of areas of the three sub-triangles in the Barycentric triangle, and thus they sum to 1. Placing the triangle in a Cartesian coordinate $\mathbf{x}^b \equiv (y^b, y^b)$, the location of any point within the triangle is a convex combination of those of the three vertices, i.e.,

$$\mathbf{x}^b = \mathbf{x}_{1c}^b C_1 + \mathbf{x}_{2c}^b C_2 + \mathbf{x}_{3c}^b C_3 \quad (\text{A.2})$$

where \mathbf{x}_{1c}^b , \mathbf{x}_{2c}^b , and \mathbf{x}_{3c}^b are the coordinates of the three vertices of the triangle (see Fig. 1). The superscript b is used to distinguish it from the coordinate system for the fluid flow problems.

While Emory[18] perturbed the Reynolds stress towards the three limiting states (the vertices of the triangle), we need to parameterize and explore the entire triangle. To facilitate parameterization with minimum artificial capping of Reynolds stresses falling outside the realizable range, we further transform the Cartesian coordinate (x^b, y^b) to the natural coordinate (ξ, η) by using the standard finite element shape functions:

$$x^b = x(\xi, \eta) = \sum_{i=1}^4 N_i(\xi, \eta) x_i^b \quad (\text{A.3a})$$

$$y^b = y(\xi, \eta) = \sum_{i=1}^4 N_i(\xi, \eta) y_i^b \quad (\text{A.3b})$$

where (x_i^b, y_i^b) are the coordinates of four vertices, and N_1 , N_2 , N_3 , and N_4 are shape functions

defined as

$$\begin{aligned} N_1(\xi, \eta) &= \frac{(1 - \xi)(1 - \eta)}{4} \\ N_2(\xi, \eta) &= \frac{(1 + \xi)(1 + \eta)}{4} \\ N_3(\xi, \eta) &= \frac{(1 + \xi)(1 - \eta)}{4} \\ N_4(\xi, \eta) &= \frac{(1 - \xi)(1 + \eta)}{4}. \end{aligned}$$

The mapping from the natural coordinate (ξ, η) to the physical coordinate (x^b, y^b) as in Eq. (A.3) is routinely used in finite element methods. However, the inverse mapping, i.e., computing the natural coordinate (ξ, η) for a given physical coordinate (x^b, y^b) , is nontrivial and uncommon due to the difficulty of solving the bilinear equation system Eq. (A.3). In this work we use the analytical results from [44] to obtain this mapping.

In summary, the Reynolds stresses field $\tilde{\boldsymbol{\tau}}^{rans}$ computed from the baseline RANS simulation are mapped to the physical interpretable variables $\tilde{k}^{rans}, \tilde{\xi}^{rans}, \tilde{\eta}^{rans}$ via the following sequence:

$$\tilde{\boldsymbol{\tau}} \xrightarrow{(1)} (\tilde{k}, \tilde{\lambda}_1, \tilde{\lambda}_2) \xrightarrow{(A.1)} (\tilde{k}, \tilde{C}_1, \tilde{C}_2) \xrightarrow{(A.2)} (\tilde{k}, \tilde{x}^b, \tilde{y}^b) \xrightarrow{\text{inv. of (A.3)}} (\tilde{k}, \tilde{\xi}, \tilde{\eta})$$

where unperturbed quantities \mathbf{v}_1^{rans} , \mathbf{v}_2^{rans} , and \mathbf{v}_3^{rans} , dependent variables λ_3 and C_3 , and superscript *rans* are omitted for simplicity of notation. Equations describing the mappings are indicated above the corresponding arrow. Equation (1) indicates eigen-decomposition and reconstruction. After the sequence of mapping, uncertainties are introduced into these transformed quantities by modeling the truth of k , ξ , η as random fields with their respective baseline results as priors (see Eq. (2)). They are subsequently used to obtain Reynolds stresses via the inverse of mapping sequence as above:

$$(k, \xi, \eta) \xrightarrow{(A.3)} (k, x^b, y^b) \xrightarrow{\text{inv. of (A.2)}} (k, C_1, C_2) \xrightarrow{\text{inv. of (A.1)}} (k, \lambda_1, \lambda_2) \xrightarrow{(1)} \boldsymbol{\tau}$$

Appendix B. Iterative Ensemble Kalman Method for Inverse Modeling

The algorithm of the iterative ensemble Kalman method for inverse modeling is summarized below. See [29] for details.

Given velocity prediction from the baseline RANS simulation \mathbf{u}^{rans} and observations with error covariance matrix R , the following steps are performed:

1. **(Sampling step)** Generate initial ensemble $\{\mathbf{x}_j\}_{j=1}^N$ of size N , where the augmented system state is:

$$\mathbf{x}_j = [\mathbf{u}^{rans}, \boldsymbol{\omega}]_j$$

2. **(Prediction step)**

- (a) Propagate the state from current state n to the next iteration level $n + 1$ with the forward model `tauFoam`, indicated as \mathcal{F} ,

$$\hat{\mathbf{x}}_j^{(n+1)} = \mathcal{F}[\mathbf{x}_j^{(n)}]$$

This step involves reconstructing Reynolds stress fields for each sample and computing the velocities from the RANS equations.

- (b) Estimate the mean $\bar{\mathbf{x}}$ and covariance $P^{(n+1)}$ of the ensemble as:

$$\begin{aligned}\bar{\mathbf{x}}^{(n+1)} &= \frac{1}{N} \sum_{j=1}^N \hat{\mathbf{x}}_j^{(n+1)} \\ P^{(n+1)} &= \frac{1}{N} \sum_{j=1}^N (\hat{\mathbf{x}}_j \hat{\mathbf{x}}_j^T - \bar{\mathbf{x}} \bar{\mathbf{x}}^T)^{(n+1)}\end{aligned}$$

3. **(Analysis step)**

- (a) Compute the Kalman gain matrix as:

$$K^{(n+1)} = P^{(n+1)} H^T (H P^{(n+1)} H^T + R)^{-1}$$

- (b) Update each sample in the predicted ensemble as follows:

$$\mathbf{x}_j^{(n+1)} = \hat{\mathbf{x}}_j^{(n+1)} + K(y - H \hat{\mathbf{x}}_j^{(n+1)})$$

4. Repeat the prediction and analysis steps until the ensemble is statistically converged.